Materials Characterization 132 (2017) 156–161

Contents lists available at ScienceDirect

Materials Characterization

journal homepage: www.elsevier.com/locate/matchar

# Direct versus indirect particle strengthening in a strong, ductile FeNiMnAlTi high entropy alloy

Zhangwei Wang[a], Arda Genc[b], Ian Baker[a,*]

[a] Thayer School of Engineering, Dartmouth College, Hanover, NH 03755, USA
[b] Thermo Fisher Scientific, 5350 NE Dawson Creek Dr. Hillsboro, OR 97124, USA

ARTICLE INFO

*Keywords:*
High entropy alloy
Dispersion hardening
Mechanical properties
SEM and TEM
HAADF imaging

ABSTRACT

In this paper, we show that the strengthening from (Ni, Al, Ti)-rich B2 particles in the recrystallized (Fe, Mn)-rich f.c.c. high entropy alloy (HEA) $Fe_{42}Ni_{12}Mn_{36}Al_8Ti_2$ arises indirectly by reducing the grain size thus providing increased Hall-Petch strengthening, rather than directly through dislocation pinning, a concept first introduced by P.M. Hazzledine (Scripta Metall. Mater. 26 (1992) 57–58). Thus, the yield strength increased from 200 MPa for the as-cast HEA to 509 MPa for the recrystallized HEA. The contributions to the increase of the yield strength were calculated to be 28 MPa from particle pinning and 281 MPa from Hall-Petch strengthening. We also show using high angle angular dark field imaging in a scanning transmission electron microscope that $Fe_{42}Ni_{12}Mn_{36}Al_8Ti_2$ exhibits no evidence of the severe lattice distortion that is a core tenet of HEAs. Both as-cast and recrystallized HEAs showed ductile fracture modes.

## 1. Introduction

Recently, a new alloy design strategy based on the maximization of configurational entropy has been proposed to produce multicomponent alloys with attractive properties [1–3]. Several $Fe_{42}Ni_{12}Mn_{36}Al_8$-based high entropy alloys (HEAs) with excellent mechanical properties have been successfully developed [4–7]. For example, a $Fe_{40.4}Ni_{11.3}Mn_{34.8}Al_{7.5}Cr_6$ HEA with a grain size of 5 μm doped with 1.1 at.% carbon exhibits an ultimate tensile strength of 1 GPa and a tensile elongation of 27% at room temperature, thus outperforming most advanced steels [8].

Thermo-mechanical treatments have been shown to be a promising way to strengthen HEAs via the enhancement from grain boundary and precipitate strengthening [8–10]. It has been shown that cold-rolling and annealing produced a fcc/B2 duplex $AlCoCrFeNi_{2.1}$ HEA with ultrafine grains of ~0.6 μm, leading to the increase of yield strength from ~620 MPa for the as-cast alloy to ~1100 MPa for the recrystallized alloy [11].

Hazzledine [12] suggested that indirect Hall-Petch strengthening (retardation of dislocations from grain boundaries), rather than direct Orowan strengthening (pinning of dislocations from particles), plays a dominate role in dispersion-hardened alloys. However, no study has been performed on HEAs to evaluate the contributions of yield strength from direct and indirect strengthening separately.

Severe lattice distortion was regarded as one of the four core effects of HEAs. It is believed that each element has a different atomic size and modulus in a HEA, which leads to a highly distorted lattice in HEAs compared with alloys with one dominant element [2]. However, there is insufficient evidence to support the existence of severely distorted lattices in HEAs [13]. Pickering and Jones [3] even proposed that such severe lattice distortion are unlikely to exist, since solid solutions are difficult to form in alloys with a very large mismatch of atomic size. Thus, a direct observation on the lattice structure based on high-resolution scanning transmission electron microscope is critical for the understanding of this issue.

In this study, we produced a novel f.c.c./B2 $Fe_{42}Ni_{12}Mn_{36}Al_8Ti_2$ HEA by adding 2 at.% Ti to the $Fe_{42}Ni_{12}Mn_{36}Al_8$ alloy. A thermo-mechanical treatment was performed on the HEA that reduced both the grain size and the precipitate size, and increased the volume fraction of precipitates, leading to a sharp increase in strength. The direct Orowan strengthening and indirect Hall-Petch strengthening in the recrystallized HEA are quantitively evaluated. We further report the atomic-scale characterization of both the f.c.c. and B2 phases in the recrystallized HEA in order to clarify the chemistry and lattice structure of each phase in the HEA.

## 2. Experimental

Arc-melting was used to cast the $Fe_{42}Ni_{12}Mn_{36}Al_8Ti_2$ HEA from elemental pieces of 99.99% Fe, 99.95% Ni, 99.9% Mn, 99.9% Al, and

* Corresponding author.
*E-mail address:* Ian.Baker@dartmouth.edu (I. Baker).

http://dx.doi.org/10.1016/j.matchar.2017.08.019
Received 12 July 2017; Received in revised form 22 August 2017; Accepted 22 August 2017
Available online 24 August 2017

99.9% Ti. An additional 5 wt% Mn was added to compensate for the evaporation loss. The ingot was melted three times to ensure a homogeneous mixture. Thermo-mechanical treatment was undertaken to recrystallize the HEA, i.e. specimens were cold-rolled to a 70% reduction in thickness with a reduction of ~5% per pass, followed by annealing at 1073 K for 8 h.

A FEI XL 30 field emission gun scanning electron microscope (SEM) operated in backscattered electron (BSE) mode at 15 keV, and a Tecnai F20 FEG transmission electron microscope (TEM) equipped with an energy dispersive X-ray spectroscopy system (EDS) operated at 200 keV were employed to examine the microstructures. The samples for SEM and TEM examination were electro-polished in 20% nitric acid in methanol at 253 K with a voltage of ~11 V and a current of ~90 mA using Stuers Tenupol 5. The grain size was determined using a linear intercept method. The volume fraction and size of precipitates were calculated from SEM images using Image J based on the contrast difference between the phases. There is no overlap of B2 particles in SEM images, which allows for accurate measurements. Approximately 100 and 600 measurements were performed for the as-cast and recrystallized HEAs, respectively. The precipitates were treated as spherical particles and the diameter of each particle was calculated from the measured area.

High angular annular dark field (HAADF) scanning TEM (STEM) imaging is conducted using a probe aberration corrected FEI Themis Z microscope at 300 keV accelerating voltage. The EDS maps are acquired using FEI Themis Z microscope equipped with a FEI Super-X™ detector system, which combines symmetrically placed four Si drift detectors (SDD) around the objective lens with a high-brightness gun. This combination provides enhanced generation of X-rays and together with high detector efficiency results in a faster mapping of larger areas in EDS maps.

Dog-bone specimens with a gauge length of ~10 mm, width of ~2.6 mm, and thickness of ~1.27 mm, polished to a mirror finish, were produced for the tensile tests. Two specimens were tested for both the as-cast and recrystallized HEA at a room temperature with an initial strain rate of $5 \times 10^{-4}\ s^{-1}$. The elongation to fracture was determined based on measurements of the gauge length before and after tests. The measured elongation was used to calibrate the displacement of the crosshead, and then strain was determined from the calibrated tensile load–displacement data. The work-hardening rate was obtained from the derivatives of the true stress–true strain curve.

## 3. Results and Discussion

The BSE images in Fig. 1 show the microstructures of the $Fe_{42}Ni_{12}Mn_{36}Al_8Ti_2$ HEA in both as-cast and recrystallized states. The as-cast HEA has a large grain size of 128 μm containing large, widely-separated, irregularly-shaped particles with the size of 4 ± 1 μm, as shown in Fig. 1a. The inserted electron backscatter diffraction (EBSD) pattern in Fig. 1a indicates that the particles have B2 structures. Fig. 1b shows that the grain size was reduced to 3 μm after the thermo-mechanical treatment. Annealing twins are also evident in Fig.1b. The wide grain boundaries in Fig. 1b suggest the presence of a second phase, but EDS scans across grain boundaries could not detect any chemistry differences there, see Fig. 2. Precipitation of the B2 phase occurred during the annealing and the volume fraction of particles increased from 4 vol% in the as-cast alloy to 11 vol% in the recrystallized alloy. After the annealing, there was a bimodal precipitate distribution with large particles (553 ± 215 nm, 3 vol%) on the grain boundaries and smaller particles (223 ± 163 nm, 8 vol%) in the grains, which were either spherical or ellipsoidal. The larger size of the grain boundary particles in the recrystallized alloy suggests that substantial particle growth occurred during the annealing, the greater diffusion rate along the grain boundaries compared to the lattice giving rise to the larger particles there. However, overall both the particles in the grain boundaries and the particles in the grain were smaller than the particles in the as-cast alloy presumably because the rolling broke up the large particles and because of the subsequent precipitation.

Fig. 3a shows the bright field (BF) TEM image for the recrystallized HEA. The precipitates were distributed in grain boundaries and inside grains. The selected area diffraction (SAD) patterns in Fig. 3 b and c show that the matrix is a f.c.c. structure, and the precipitate is a B2 structure, respectively.

The microstructure of the $Fe_{42}Ni_{12}Mn_{36}Al_8Ti_2$ HEA is sensitive to the processing condition: annealing produces precipitation in the HEA, similar behavior that has been observed in a single f.c.c. HEA $Fe_{40.4}Ni_{11.3}Mn_{34.8}Al_{7.5}Cr_6$ [8] and in a two-phase f.c.c./B2 $Fe_{36}Ni_{18}Mn_{33}Al_{13}$ [14]. The annealing led to precipitation of a B2 phase in both alloys with the volume fraction of precipitates increasing as the annealing time increased. The B2 precipitates in $Fe_{42}Ni_{12}Mn_{36}Al_8Ti_2$ clearly exerted a strong pinning force on the grain boundaries during recrystallization, resulting in a very fine grain size of 3 μm. Such pinning effect from the second phase has also been seen in a $Fe_{28.2}Ni_{18.8}Mn_{32.9}Al_{14.1}Cr_6$ HEA [5] and a $AlCoCrFeNi_{2.1}$ HEA [11].

The atomic structures of the phases in the recrystallized HEA were examined using a high-resolution STEM equipped with a high angle angular dark field (HAADF) detector. Fig. 4a shows a HAADF-STEM image of both f.c.c. and B2 phase in the recrystallized HEA. The f.c.c. matrix and B2 precipitate have a completely different orientation, and thus have an incoherent interface. The orientation relationship between f.c.c. and B2 phases in FeNiMnAl alloys have previously been determined by Liao and Baker [15]. The Krudjumov-Sachs orientation relationship between the f.c.c. and B2 phases was observed in a drop-cast eutectic $Fe_{30}Ni_{20}Mn_{35}Al_{15}$ alloy, whereas the f.c.c. $(1\bar{1}2)$ // B2 (011); f.c.c. $[1\bar{1}1]$ // B2 $[1\bar{1}1]$ and f.c.c. $(0\bar{1}1)$ // B2 (001); f.c.c. [011] // B2 $[\bar{1}\bar{1}0]$ relationships were exhibited in an arc-melted eutectic alloy.

The atomic columns for f.c.c. and B2 phases are shown at higher magnification in Fig. 4 b and c, respectively. Both f.c.c. and B2 phase in the $Fe_{42}Ni_{12}Mn_{36}Al_8Ti_2$ HEA exhibit nearly perfect crystal lattices without any severe lattice distortions, which is consistent with the lack of such distortions observed using high-resolution TEM in a CoCrCuFeNiAl$_{0.5}$ HEA [16]. Recently, the core effect of severe lattice distortions in HEAs has been questioned since many studies indicated that the

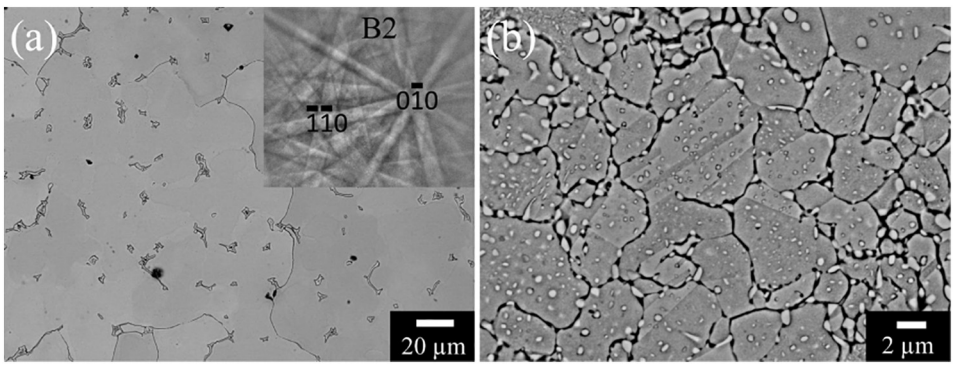


**Fig. 1.** BSE images of the microstructures of (a) as-cast and (b) recrystallized $Fe_{42}Ni_{12}Mn_{36}Al_8Ti_2$ (the inserted EBSD pattern in (a) shows that particles are B2 phases). Note that factor of nearly 10 change in scale between (a) and (b).